J. Phys.: Condens. Matter **23** (2011) 295502 (10pp) doi:10.1088/0953-8984/23/29/295502

Effect of strain on the thermoelectric properties of silicon: an *ab initio* study

N F Hinsche[1,3], I Mertig[1,2] and P Zahn[1]

[1] Institut für Physik, Martin-Luther-Universität Halle-Wittenberg, D-06099 Halle, Germany
[2] Max-Planck-Institut für Mikrostrukturphysik, Weinberg 2, D-06120 Halle, Germany

E-mail: nicki.hinsche@physik.uni-halle.de

Received 10 March 2011, in final form 9 June 2011
Published 8 July 2011
Online at stacks.iop.org/JPhysCM/23/295502

Abstract
On the basis of detailed first-principles calculations the anisotropic thermoelectric transport properties of biaxially strained silicon were studied with the focus on a possible enhancement of the power factor. Electron as well as hole doping was examined in a broad doping and temperature range. In the low temperature and low doping regime an enhancement of the power factor was obtained for compressive and tensile strain in the electron-doped case, and for compressive strain in the hole-doped case. In the thermoelectrically more important high temperature and high doping regime a slight enhancement of the power factor was only found for the hole-doped case under small biaxial tensile strain. The results are discussed in terms of band structure effects. An analytical model is presented to understand the fact that the thermopower decreases if degenerate bands are energetically lifted due to a strain-induced redistribution of states.

(Some figures in this article are in colour only in the electronic version)

1. Introduction

Thermoelectrics convert heat into electric current, and vice versa. Known for more than 60 years, thermoelectrics currently attracts a great deal of attention [1–4]. With nearly 90% of the world's power being generated by low efficiency heat engines, thermoelectric modules could potentially convert parts of this wasted heat into electricity. Their conversion efficiency can be stated by the figure of merit:

$$ZT = \frac{\sigma S^2}{\kappa_{\mathrm{el}} + \kappa_{\mathrm{ph}}} T, \tag{1}$$

where σ is the electrical conductivity, S is the thermopower, and κ_{el} and κ_{ph} are the electronic and phononic contributions to the thermal conductivity, respectively. The numerator of equation (1) is called the power factor $\mathrm{PF} = \sigma S^2$.

While $ZT > 1$ was challenging to be reached in the last decades, nowadays nanostructured thermoelectrics enable even larger values of ZT [5–7]. Unfortunately, those materials are often based on environmentally unfriendly lead, tellurium or selenium compounds and are therefore hard to integrate in semiconductor electronics.

[3] Author to whom any correspondence should be addressed.

Silicon, the cradle of modern semiconductor electronics, is nonpolluting, readily available, cheap and perfectly integrated in the present electronics infrastructure. While silicon has been stated as an inefficient thermoelectric in the past due to its enormous thermal conductivity [8], recent experiments and theory revealed that nanostructuring could lead to thermoelectric efficiencies comparable to state-of-the-art commercial thermoelectric materials [9–13].

As in nanostructured materials mechanical strain plays an important role; this paper will focus on the influence of biaxial strain on the electronic thermoelectric transport properties of bulk silicon, which might occur in rolled-up and layered Si heterostructures [14–17]. It is well known, that similar strain physics, e.g. band splitting and band deformation, are expected for strained three-dimensional systems, as well as for one and two-dimensional silicon devices in complex strain states. A comprehensive overview on this can be found in [14]. In detail these common strain physics affect the electronic carrier transport depending on the dimensionality, temperature and doping density. The question to be answered in this paper will be whether tensile or compressive strain will lead to an enhancement or reduction of the power factor in silicon under a certain doping and temperature environment. Besides our interest in the high temperature thermoelectric application of

strained silicon we want to emphasize the possible importance of our results in the low temperature regime for the metal-oxide–semiconductor device community, where the knowledge of the thermoelectric properties of silicon under strain could help to understand parasitic effects in these devices. In the low doping regime at low temperature, an enhancement of one part of the power factor, namely the electrical conductivity, under externally applied strain, was found and heavily investigated in the last few decades [18, 19, 14]. For this purpose this paper will be organized as follows. In section 2 we introduce our first-principles electronic structure calculations based on density functional theory and the transport calculations based on the solution of the linearized Boltzmann equation. With this knowledge we start the discussion of the thermoelectric transport properties of unstrained bulk silicon (section 3.1) and present afterwards the influence of biaxial strain on the electron-or hole-doped case of silicon in section 3.2. In the last paragraphs 3.3 and 4 the optimal power factor under strain due to variation of doping is determined and analyzed, while estimations of the possible figure of merit are given.

2. Methodology

Our approach is based on two ingredients: first-principles density functional theory calculations (DFT), as implemented in the Quantum Espresso package [20], and an in-house developed Boltzmann transport code [21] to calculate the thermoelectric transport properties.

2.1. Electronic structure

In a first step the band structure of the strained and unstrained Si was calculated using the generalized gradient approximation (GGA) and the PBE (Perdew–Burke–Emzerhof) exchange correlation functional [22]. Fully relativistic and norm-conserving pseudopotentials [23] were used to treat the spin–orbit splitting of the Si valence bands in a correct way. The calculations were performed with the experimental lattice constant $a = 5.434$ Å for a face-centered tetragonal eight-atom unit cell. The in-plane biaxial strain is simulated by changing the c/a ratio but keeping the cell volume constant. Throughout the paper the biaxial strain will be given in units of the relative change of the in-plane lattice constant as $\Delta a/a_0 = a/a_0 - 1$. That means tensile strain considers changes $\Delta a/a_0 > 0$, while compressive strain means $\Delta a/a_0 < 0$.

As expected, our DFT calculations underestimate the size of the bandgap at zero temperature and do not reproduce the temperature dependence of the gap. For this purpose we included a temperature-dependent scissor operator [24], so that the strain- and temperature-dependent energy gap E_g in electronvolts becomes

$$E_g\left(T, \frac{\Delta a}{a_0}\right) = E_g\left(T = 0, \frac{\Delta a}{a_0}\right) + U_{GGA} - \frac{4.73 \times 10^{-4} T^2}{T + 636}, \tag{2}$$

where $E_g(T = 0, \frac{\Delta a}{a_0})$ is the zero-temperature gap obtained by our self-consistent DFT calculations and $U_{GGA} = 0.57$ eV is a static correction to fulfil the experimental low temperature gap. The third part of equation (2) is the correction of the temperature dependence of the bandgap [25] in a wide temperature range with T given in K.

2.2. Boltzmann transport

With the converged results from the first step we are now able to obtain the thermoelectric transport properties by solving the linearized Boltzmann equation in the relaxation time approximation (RTA) [21]. Boltzmann transport calculations for thermoelectrics have been carried out for quite a long time and show reliable results for metals [26–29] as well as for wide- and narrow-gap semiconductors [30–33]. In here the relaxation time is assumed to be constant with respect to wavevector k and energy on the scale of $k_B T$. This assumption is widely used for metals and doped semiconductors. The constant relaxation time is a big advantage for the calculation of the thermopower S without any adjustable parameter, while lacking any doping or temperature dependence of τ. For unstrained silicon, doping-dependent relaxation times of the order of 15–150 fs for electron doping and 6–65 fs for hole doping could be estimated from experiments in [34]. To concentrate on the band structure effects we assume the relaxation time does not depend on strain, while it was shown that under strain the dominant scattering process varies: for unstrained Si, the room temperature scattering is dominated by optical phonons, i.e. intervalley scattering, whereas for strained Si, this scattering process is less efficient [35, 36].

The temperature- and doping-dependent thermopower in- and cross-plane is defined as

$$S_{\perp,\parallel} = \frac{1}{eT} \frac{\mathcal{L}^{(1)}_{\perp,\parallel}(\mu, T)}{\mathcal{L}^{(0)}_{\perp,\parallel}(\mu, T)}, \tag{3}$$

where

$$\mathcal{L}^{(n)}_{\perp,\parallel}(\mu, T) = \frac{\tau}{(2\pi)^3} \times \sum_\nu \int \mathrm{d}^3k (v^\nu_{k,(\perp,\parallel)})^2 (E^\nu_k - \mu)^n \left(-\frac{\partial f_{(\mu,T)}}{\partial E}\right)_{E=E^\nu_k} \tag{4}$$

is the transport distribution function as termed by Mahan and Sofo [37], for a given chemical potential μ at temperature T and carrier concentration N determined by an integration over the density of states $n(E)$:

$$N = \int_{\mu-\Delta E}^{\mathrm{VB^{max}}} \mathrm{d}E n(E)[f_{(\mu,T)} - 1] + \int_{\mathrm{CB^{min}}}^{\mu+\Delta E} \mathrm{d}E n(E) f_{(\mu,T)}, \tag{5}$$

where $\mathrm{CB^{min}}$ is the conduction band minimum and $\mathrm{VB^{max}}$ is the valence band maximum. As can be seen straightforwardly from equations (3) and (4) the electrical conductivity σ is then given by

$$\sigma_{\perp,\parallel} = 2e^2 \mathcal{L}^{(0)}_{\perp,\parallel}(\mu, T). \tag{6}$$

The Fermi surface integration, which is requested in equation (4), is performed within an extended tetrahedron method [38–40] interpolating the calculated eigenvalues E^ν_k on a mesh of at least 13 950 k points in the irreducible part of the Brillouin zone. $\mathcal{L}^{(0)}_{\perp,\parallel}(E, T = 0)$ was determined on a fine energy mesh with a step width of 1 meV. Convergence tests

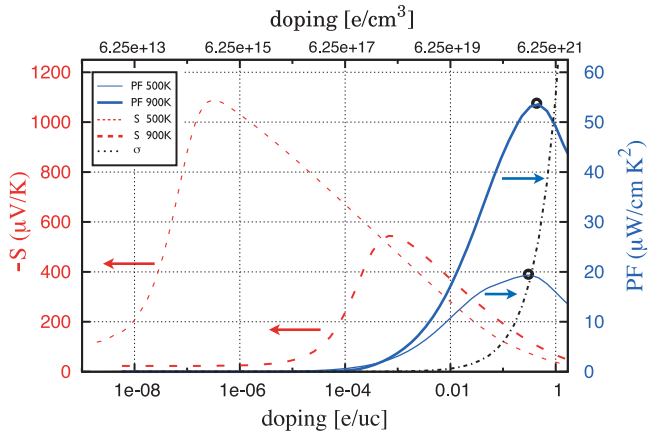

Figure 1. In-plane thermopower (red dashed lines, refer to left scale, red units) and power factor (blue solid lines, refer to right scale, blue units) for unstrained, electron-doped silicon in dependence on the doping level. Furthermore the doping dependence of the electrical conductivity is given as a dashed–dotted line in arbitrary units. The maxima of the power factor are marked by black open circles.

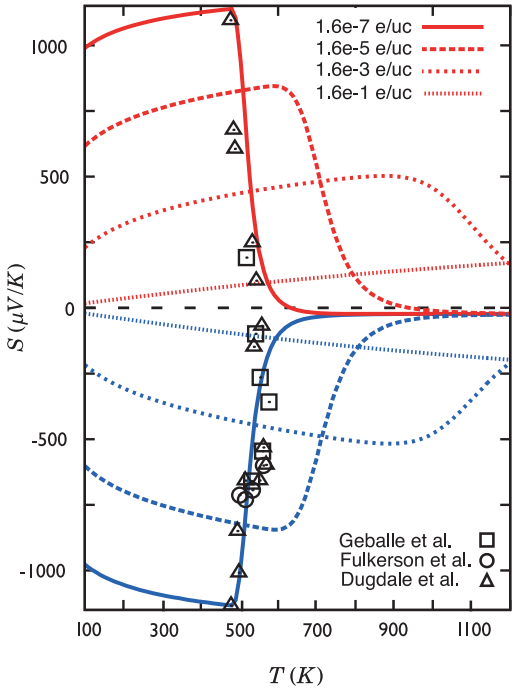

Figure 2. Thermopower for unstrained silicon in dependence on doping and temperature. Electron doping refers to the blue lines in the lower part of the figure, while red lines refer to hole doping and positive values of the thermopower. Experimental data (squares, circles and triangles) from [42–44] are given for comparison.

confirmed that the calculation of the electrical conductivity and the thermopower at a given temperature via equations (6) and (3) requires $\mathcal{L}^{(0)}_{\perp,\parallel}(E, T = 0)$ for quite a large range. Convergence of the integrals (4) and (5) was achieved with an adaptive integration method for $2\Delta E \geqslant 20 k_B T$ in the limit of low carrier concentrations $N \leqslant 1 \times 10^{14}$ cm^{-3}.

3. Thermoelectric transport

3.1. Unstrained case

Since the thermoelectric transport properties of the strained silicon will always be discussed in comparison with the unstrained case, we will provide an insight into the transport properties of the unstrained silicon. In figure 1, the thermopower and the power factor are shown for two different temperatures (500 and 900 K) in a wide doping range. The qualitative behavior of the electrical conductivity is indicated by the dashed–dotted line to emphasize the trend of the resulting power factor. The picture is well known for the interrelation of electronic transport and the thermoelectric properties of semiconductors [41, 1]. At constant temperature the thermopower (cf the red dashed lines in figure 1) decreases at very low and higher doping levels and reaches a maximum in between [41].

As can be seen from figure 1 the thermopower reaches a maximum around an electron carrier concentration of 1×10^{15} cm^{-3} at 500 K, while the maximum at 900 K is shifted to a larger doping level of 1×10^{18} cm^{-3}. Besides that, the maximum of the more relevant power factor (cf blue solid lines in figure 1, optimal values indicated by black open circles) is shifted to huge electron carrier concentrations of about 1×10^{21} cm^{-3}. This is determined by the linear increase of the electrical conductivity with increasing charge carrier concentration. Obviously, there is not much space to optimize the power factor with respect to temperature and charge carrier concentration for unstrained silicon. We will focus on this optimization in more detail in section 3.3. The complex dependence of the thermopower on temperature and doping is shown in figure 2 for electron- and hole-doped unstrained silicon at different doping concentrations. For low temperatures and doping levels the thermopower reaches values of 1000 μV K^{-1} and above, which is caused by the location of the chemical potential near the band edges. The denominator of equation (3), proportional to the electrical conductivity, is small, while the nominator is large and the thermopower becomes maximal. At fixed charge carrier concentration the position of the chemical potential is shifted towards the middle of the gap with increasing temperature. The denominator in equation (3) decreases, because it is mainly determined by the opposite contributions of the tails of the derivative of the Fermi–Dirac distribution function with respect to the valence and conduction bands (equation (4), $n = 1$). At a distinct temperature of about 500 K the thermopower rapidly vanishes. At this temperature the electronic transport enters into the bipolar intrinsic regime. To emphasize the relevance of our calculations experimental results for merely pure silicon in the intrinsic transport regime are added in figure 2. We want to point out that the thermopower does not vanish at all, but converges to small negative values for electron, as well as for hole doping. At large charge carrier concentrations of about 0.16 e/uc (dotted lines in figure 2), where the power factor becomes large, the thermopower grows linearly with temperature up to values of 150 μV K^{-1} at 1000 K. In the heavy doped regime the chemical potential is located deep in the bands and equation (3) qualitatively

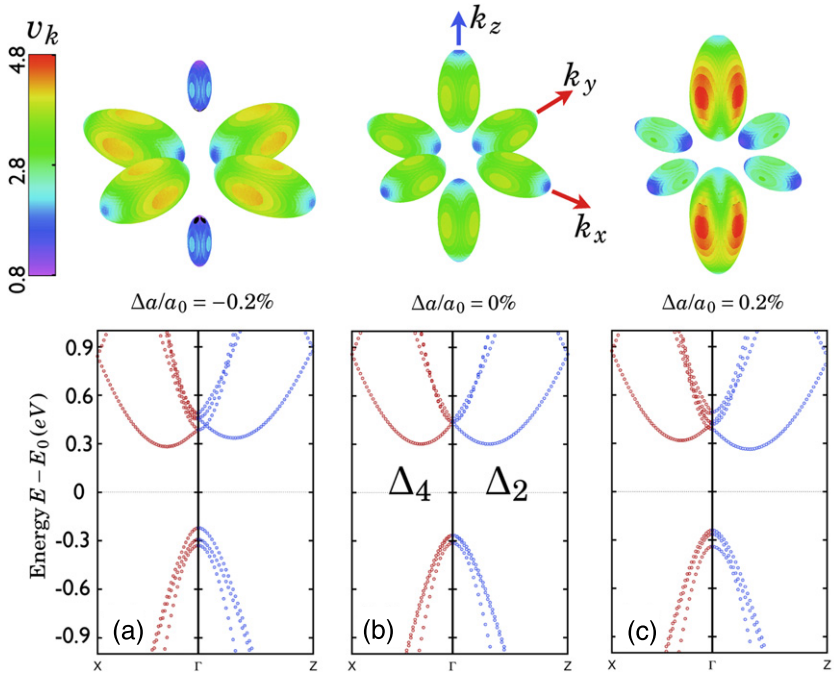

Figure 3. Fermi surfaces of electron-doped silicon under compressive strain (left), no strain (middle) and tensile strain (right). On the Fermi surfaces the absolute value of the group velocities are plotted in units of 0.08×10^6 m s^{-1}. As reference the band structure on two high symmetry lines is given below. The doping corresponds to additionally 0.01 electrons per unit cell which causes carrier densities of 6.25×10^{19} cm^{-3}.

coincides with the well-known MOTT relation $S \propto \frac{\mathrm{d}\ln\sigma(E)}{\mathrm{d}E}|_{E=\mu}$ for the thermopower in RTA [45].

3.2. Optimization of the power factor by strain

3.2.1. Electron doping. Having provided a general view on the thermoelectric transport properties of unstrained silicon above, we will now focus on the effect of biaxial strain on those properties. The results are presented in comparison to the unstrained case, starting with the electron-doped case, followed by the hole-doped case in section 3.2.2.

In strain-free bulk silicon, as introduced in section 3.1, the conduction band minimum (CBM) consists of six equivalent valleys on the Γ–X high symmetry line as shown in the middle panel of figure 3(b). The Fermi surface pockets corresponding to these valleys are shown on top, with the absolute value of the carrier's group velocity, v_k entering equation (4), plotted in color on the surface. The color code gives v_k in units of 0.08×10^6 m s^{-1}. By applying biaxial in-plane strain, the six CBM valleys are energetically split into two groups: four degenerate in-plane Δ_4 valleys and two degenerate cross-plane Δ_2 valleys (see figures 3(a) and (c)). While the number of electrons is fixed, the different sizes of the ellipsoidal pockets are caused by a change of occupation numbers under strain. The color code indicates the overall smaller Fermi velocities on the small pockets and in particular on the principal axis of the pockets, whereas larger velocities are found for states propagating perpendicular to the principal pocket axis. In figure 4 the thermoelectric transport properties of biaxial strained silicon for two fixed electron doping regimes are shown. First, we consider the left column (figures 4 (a)–(c)), which shows the electrical conductivity σ, the thermopower S and the resulting power factor $\mathrm{PF} = \sigma S^2$ for a low electron doping of 1.6×10^{-7} e/uc and a low temperature of 100 K. For this doping and temperature value a large enhancement of up to 35% of the electrical conductivity is obtained for the in-plane component $\sigma_\parallel$ at low tensile strain and for the cross-plane component $\sigma_\perp$ at small compressive strain. $\sigma_\perp$ drops noticeable under small tensile strain up to 30% of the unstrained case, while $\sigma_\parallel$ experiences a slight drop down to 83% under small compressive strain, respectively.

With the conduction bands of silicon behaving parabolically near the band edges, the calculated transport properties can be understood for small charge carrier concentrations and low temperatures in terms of effective masses and occupation number redistributions (see [35]). With increasing tensile strain the Δ_4 bands lift up and the occupied states from the higher bands are transferred to the lowered Δ_2 bands (compare figure 3(c)). At a certain tensile strain the Δ_4 pockets are completely depleted and the maximally occupied Δ_2 states solely contribute to the transport. In a simplified consideration one can estimate the relative change in the electronic conductivity from the relative change in the effective electron mass. As reported earlier [35] it is $m_{\perp,\Delta_2} = m_{\perp,\Delta_4} = 0.205$ and $m_{\parallel,\Delta_2} = m_{\parallel,\Delta_4} = 0.926$, whereas the masses are in units of the free-electron rest mass. For the in-plane component $\sigma_\parallel$ of the electrical conductivity at sufficient tensile strain only the lowered Δ_2 bands contribute with their perpendicular mass $m_{\perp,\Delta_2}$. With the notation

$$\frac{1}{m_0} = \frac{1}{6}\left(\frac{2}{m_{\parallel,\Delta_4}} + \frac{2}{m_{\perp,\Delta_4}} + \frac{2}{m_{\perp,\Delta_2}}\right) = \frac{1}{0.277}, \qquad (7)$$

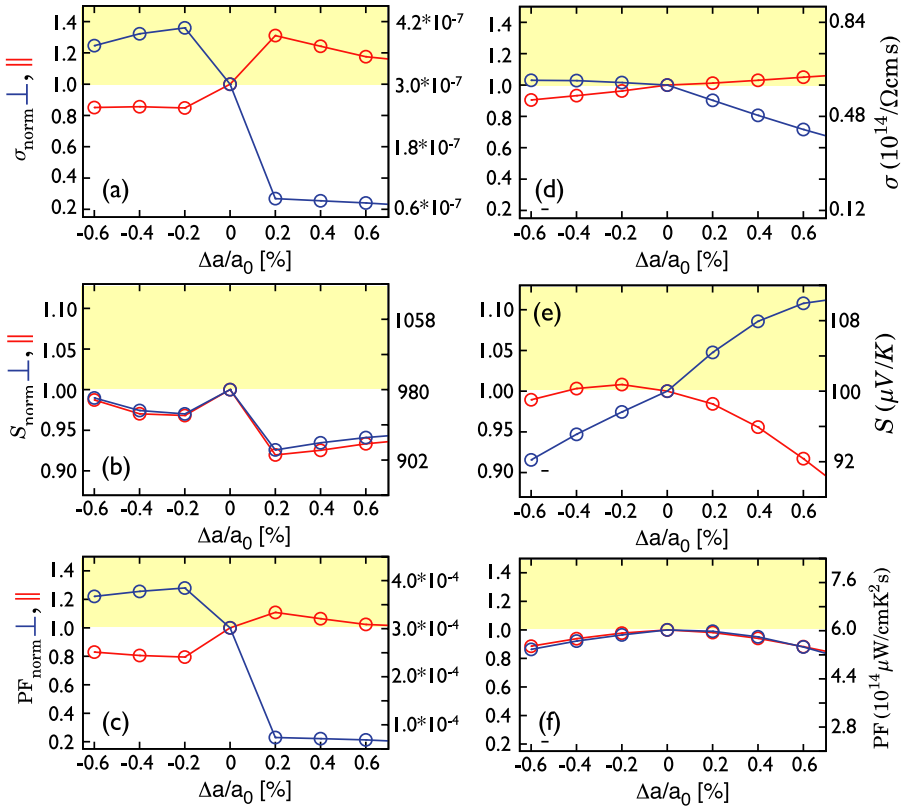

Figure 4. Anisotropic thermoelectric transport properties for fixed temperature and electron doping concentrations in dependence on compressive and tensile strain. Left panels ((a)–(c)) correspond to an electron doping of 1.6×10^{-7} e/uc at a temperature of 100 K, while the right panels refer to an electron doping of 0.48 e/uc at a temperature of 900 K. On the left axis of each figure the relative value compared to the unstrained case is shown, while on the right axis the absolute values are given. Electrical conductivity ((a), (d)) and power factor ((c), (f)) are presented in units of the relaxation time τ.

the normalized asymptotic value becomes

$$\frac{1}{2}\left(\frac{2}{m_{\perp,\Delta_2}}\right)m_0 = 1.35 \tag{8}$$

For the in-plane component $\sigma_\parallel$ of the electrical conductivity at compressive strain only the four pockets of the lowered Δ_4 bands contribute equally with their parallel and perpendicular mass:

$$\frac{1}{4}\left(\frac{2}{m_{\parallel,\Delta_4}} + \frac{2}{m_{\perp,\Delta_4}}\right)m_0 = 0.83. \tag{9}$$

For the cross-plane conductivity $\sigma_\perp$ at tensile strain it is

$$\frac{1}{2}\left(\frac{2}{m_{\parallel,\Delta_2}}\right)m_0 = 0.30, \tag{10}$$

whereas at compressive strain $\sigma_\perp$ becomes

$$\frac{1}{2}\left(\frac{2}{m_{\perp,\Delta_2}}\right)m_0 = 1.35. \tag{11}$$

Since the power factor is composed of σ and S we analyze the influence of strain on the thermopower as well. In the low temperature and doping regime (figure 4 left panel) no enhancement of thermopower at either compressive or tensile strain could be found. It can be seen, that for tensile strain the thermopower decreases by about 10%, while for compressive strain a drop of about 5% is found. The difference between the in-plane and cross-plane thermopower is marginal. In terms of MOTTS formula [45] it means that the energy dependence of $\mathcal{L}^{(0)}_{\perp,\parallel}(E,T)$ and $\mathcal{L}^{(1)}_{\perp,\parallel}(E,T)$ is almost the same. Nevertheless it is interesting to understand why the thermopower of silicon is reduced under strain and why the decay changes for tensile and compressive strains.

For qualitative understanding of our *ab initio* results we apply a free-electron model to discuss the thermopowers behavior on biaxial strain. The strain-dependent electrical conductivity at zero temperature was modeled as proposed by [35] and then the thermopower was calculated by the MOTTS relation in RTA [45]. Figure 5 shows the resulting thermopower under tensile and compressive strain for a small (dashed line) and a five times larger charge carrier concentration (solid line). For small charge carrier concentration the thermopower rapidly drops to constant values of 48% for tensile and 76% for compressive strain, respectively. We note that the maximum of S which is increased by 4% compared to the unstrained case is not located at zero strain and is shifted to very small values of compressive strain. This behavior is more pronounced for the large charge carrier concentration, where the maximum of the thermopower becomes wider and is shifted to values of -0.25 % compressive strain. Again the enhancement reached for S is about 4% and the asymptotic values remain

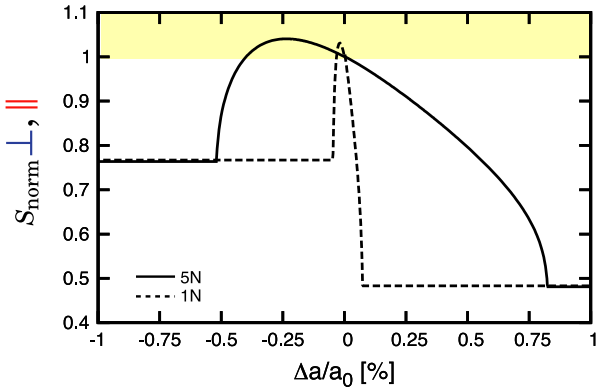

Figure 5. Analytical dependence of the thermopower on biaxial strain for different electron charge carrier concentrations, small charge carrier concentration (dashes lines) and increased charge carrier concentration by a factor of five (solid lines).

unchanged with doping. We note that for the calculation of the thermopower the influence of the effective masses completely cancels. For this reason neither for the *ab initio* nor the analytic calculation was a noticeable difference of the in-plane and cross-plane thermopower found. The different saturation values of the thermopower under tensile and compressive strain again, however, can be explained in terms of a redistribution of electrons. For free electrons at $T = 0$ the electrical conductivity $\sigma \propto E^{3/2}$ and the resulting thermopower $S \propto E^{-1}$. The amount of charge carriers in one spin band is given by $N \propto E^{3/2}$. With the MOTTS relation $S \propto N^{-2/3}$. As stated before in this paper under sufficient tensile strain only the twofold-degenerated Δ_2 pockets are occupied compared to the sixfold-degenerated CBM pockets in the unstrained case, so the occupation of every pocket increases by a factor of 3. One directly yields $S_{tens.}/S_0 = (\frac{6}{2})^{-2/3} = 0.48$. For compressive strain only the fourfold-degenerated Δ_4 pockets contribute, so it is $S_{comp.}/S_0 = (\frac{6}{4})^{-2/3} = 0.76$. The fact that, for larger charge carrier concentration, larger strain has to be applied to reach these limits, is linked to the fact that higher strain is required to reach a complete redistribution of states into either the Δ_2 or Δ_4 pockets. As a consequence of the discussed results we see in figure 4(c) an enhancement of the power factor in cross-plane direction up to 27% at small compressive strain, while the in-plane power factor is only marginally enhanced by about 5% under low tensile strain. In-plane transport under tensile strain at low doping and low temperature plays an important role in silicon-based devices. Within figure 4(c) it is obvious that the strain-induced influence of the power factor on this transport will play a minor role. We want to point out that the results on the thermopower discussed above are generally valid for all systems with degenerate occupied bands. Lifting of the degeneracy causes redistribution of electrons and reduction of the thermopower. While the low temperature and low doping case was convenient to provide some general findings on an analytical level, we will now focus on the high temperature and high doping regime (see figure 4 left panels) where the power factor might be suitable for thermoelectric application (see also figure 1). At a temperature of 900 K the electronic band structure on a width of at least $\pm\Delta E = \pm 770$ meV around the position of the chemical potential has to be included, which makes a description of the electronic transport properties within a spherical band picture impossible. Rather than providing analytical quantities a more qualitative description of our *ab initio* calculations will be given instead. The electrical conductivity in figure 4(d) states the same qualitative tendencies for $\sigma_\parallel$ and $\sigma_\perp$ as derived for the low temperature case. As a consequence of the high temperature and the related broadening of the Fermi–Dirac distribution in equations (4) and (5) as well as the high charge carrier concentration the redistribution of states as described before is not completed for the strain values considered here. The analytical limits for the enhancement of $\sigma_\parallel$ and $\sigma_\perp$ for the given high doping and temperature should be achieved for biaxial strains of at least $\Delta a/a_0 = \pm 3\%$, respectively. It is worth mentioning that the absolute value (cf right scales in figures 4(a) and (d)) of the electrical conductivity is raised enormously compared to the low doping case as expected. As a consequence, the power factor rises absolutely but unfortunately no enhancement via strain was obtained. The strain-dependent behavior of the thermopower as shown in figure 4(e) compensates the behavior of the electrical conductivity. In the high-doping–high-temperature regime the thermopower shows a noticeable anisotropy between in-plane and cross-plane components. While the in-plane component $S_\parallel$ confirms our analytical predictions for high doping (see the black solid line in figure 5) and even shows the shifted maximum to compressive strain, the cross-plane component $S_\perp$ does not follow the analytical model. This might be explained by multiband effects and nonparabolic bands, with the latter being more relevant in the cross-plane direction. The overall resulting power factor summarized in figure 4(f) shows, however, no significant anisotropy. Furthermore no enhancement by biaxial strain could be obtained; in contrast a decrease of about 20% occurs.

3.2.2. Hole doping. We will now focus in more detail on the thermoelectric properties of hole-doped biaxially strained silicon as presented in figure 6. Under full relativistic treatment the three valence bands next to the VBM at the Γ-point are the heavy hole (HH), light hole (LH), and spin–orbit split-off (SO) hole. While the HH and LH are degenerate, the SO lies 44 meV apart (see figure 3 middle panel). Under biaxial tensile or compressive strain, the valence bands become highly anisotropic and a crossover between bands occurs so that they even lose their original meaning [46]. It was shown that mechanical deformation-induced changes in the band structure offers potential for significant enhancement of the hole mobility [47]. Nevertheless, a straightforward explanation of the *ab initio* calculations as done for the electron-doped case is not any longer possible. Actually tensile and compressive biaxial strain does not only cancel the degeneracy of the heavy and light hole bands, which will cause reduced intervalley phonon scattering, but it also leads to a smaller effective conductivity mass and a further depletion of the uppermost hole band [14, 48]. Similarly to the electron-doped case in figure 6 the thermoelectric transport properties for hole-doped silicon under the influence of biaxial strain are shown for

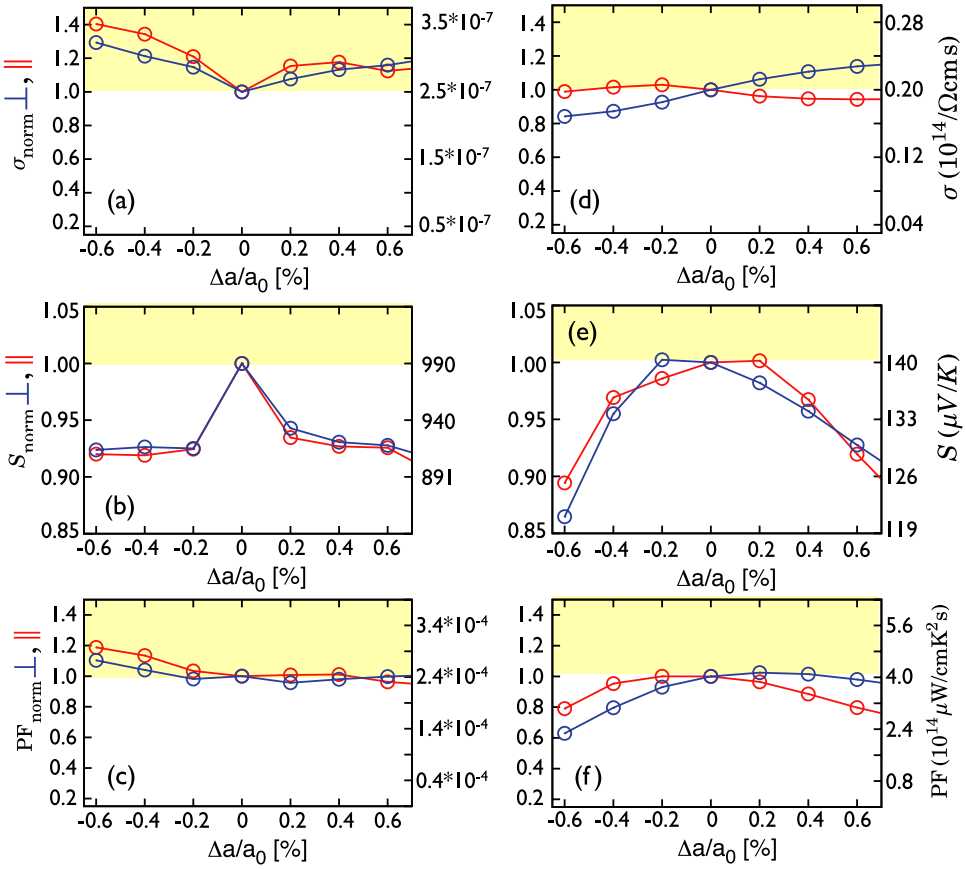

Figure 6. Anisotropic thermoelectric transport properties for fixed temperature and hole doping concentrations in dependence on compressive and tensile strain. Left panels ((a)–(c)) correspond to a hole doping of 1.6×10^{-7} h/uc at a temperature of 100 K, while right panels refer to a hole doping of 0.16 h/uc at a temperature of 900 K. On the left axis of each figure the relative value compared to the unstrained case is shown, while on the right axis absolute values are given. Electrical conductivity ((a),(d)) and power factor ((c),(f)) are presented in units of the relaxation time τ.

a fixed low doping, low temperature in figures 6(a)–(c) and fixed high doping, high temperature regime in figures 6(d)–(f). At low temperature and slight doping an increase of the electrical conductivity was found for tensile as well as for compressive strain for the in-plane component $\sigma_{\parallel}$ and the cross-plane component $\sigma_{\perp}$, while biaxial compressive strain tends to favor the enhancement of σ. As shown in figure 6(b) the thermopower for hole-doped silicon again experiences a drop of nearly 7% under compressive and tensile strain. A possible explanation for the almost symmetric drop of the thermopower under compressive and tensile strain might again be related to the number of bands being occupied. At small doping for compressive and for tensile biaxial strain the primarily occupied HH and LH split and only the upper hole band is depleted and dominates the character of the transport properties [14, 48]. Extending our analytical findings for the electron-doped case one would expect that $S_{\text{tens./compress.}}/S_0 = (\frac{2}{1})^{-2/3} = 0.63$. Through the counteracting behavior of electrical conductivity and thermopower under strain, again no enhancement of the power factor could be found (cf figure 6(c)). Only under strong compressive biaxial strain a significant enhancement is visible in the low temperature/low doping case. In the high doping and temperature regime not only does the upper hole band plays an important role in transport, but furthermore the former HH, LH and SO have to be mentioned. As shown in figure 6(d) an enhancement of around 10% compared to the unstrained case can be found for the cross-plane component $\sigma_{\perp}$ under small tensile strain. For the in-plane electrical conductivity $\sigma_{\parallel}$ under compressive strain only a marginal influence on the strain can be reported. The thermopower shows a small anisotropy of the in-plane and cross-plane components. While the thermopower is mainly decreased for compressive or tensile strain, we again see a broadening of the thermopower drop in dependence on the applied strain with respect to the low doping regime. Besides the absolute values of the power factor being around 30% smaller than in the electron-doped case (compare figures 4(f) and 6 (f)), a slight enhancement under thermoelectrically relevant doping and temperature conditions could be found for the cross-plane power factor $PF_{\perp}$ under small tensile strain (see figure 6(f)).

3.3. Optimization of the power factor by doping

While up to this point the power factor and the incorporated thermoelectric transport properties were studied for fixed temperature and charge carrier concentration in dependence on the applied biaxial strain, we want to gain further insight

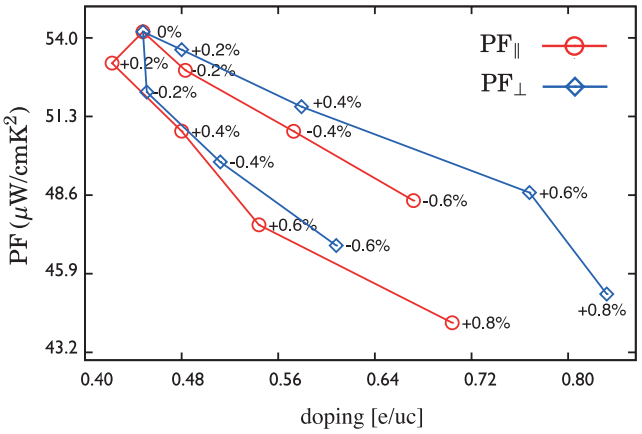

Figure 7. Anisotropic power factor optimized by the carrier concentration at given strain state for electron-doped silicon. The in-plane (cross-plane) power factors are drawn as red circles (blue diamonds). Lines are shown to guide the eyes. The temperature is fixed at 900 K.

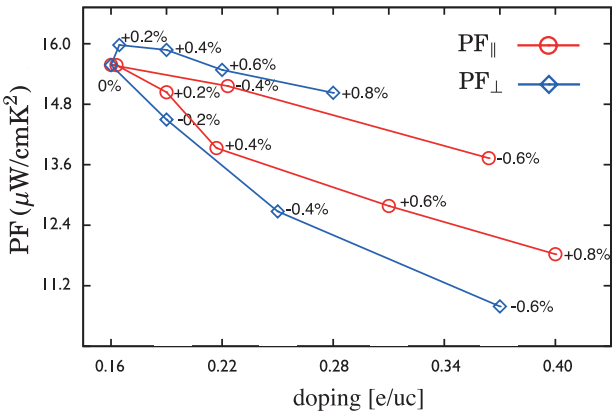

Figure 8. Same as figure 7 but optimized for hole doping.

into the doping dependence. Therefore the amount of charge carrier concentration to optimize the power factor $PF_\parallel$ and $PF_\perp$ at given strain and fixed temperature of 900 K was determined. This temperature seems to be a common temperature for thermoelectric application of silicon-based devices. Figures 7 and 8 represent the results for the electron- and hole-doped case, respectively.

From figure 7 it becomes clear that an enhancement of the power factor by sufficiently high electron doping cannot be stated. With increasing biaxial strain the in-plane and cross-plane thermopower decreases compared to the unstrained case. It is worth mentioning that the charge carrier concentration has to be increased for increasing tensile and compressive biaxial strain to achieve the optimal power factor under the certain strain condition. Nevertheless, even for a raised optimal charge carrier concentration the power factor drops to about 80% of the value of the unstrained case for the largest strain values considered here. As an interesting fact one can see that under tensile strain the cross-plane power factor $PF_\perp$ is always larger than the in-plane component $PF_\parallel$, while under compressive strain it is the other way around and $PF_\perp$ is smaller than $PF_\parallel$. In contrast to heavily electron-doped silicon an enhancement of the power factor could be found for hole-doped silicon, as shown in figure 8. Nevertheless, the enhancement is limited to the cross-plane contribution $PF_\perp$. Here we find an enhanced $PF_\perp$ under small tensile strain of $\Delta a/a_0 = 0.2\% \ldots 0.4\%$, while for tensile strain of 0.6% a value of the cross-plane power factor similar to the unstrained case is reached. We note that the charge carrier concentrations, which are necessary to optimize the power factor in the hole doping case, are about three times smaller than in the related electron doping case. Even though an enhancement of the cross-plane power factor under optimized hole doping and tensile strain can be found, unfortunately the absolute values of the power factor are sufficiently smaller than the absolute value of the $PF_\parallel$ and $PF_\perp$ of electron-doped silicon under all strain conditions examined here.

4. Tendencies on figure of merit

To evaluate tendencies of the figure of merit we are going to include and discuss experimental results for the lattice thermal conductivity κ_{ph}, which adds up to our calculated electronic thermal conductivity κ_{el} for the total thermal conductivity κ. Involving the transport distribution function in equation (4) the electronic contribution to the thermal conductivity is calculated as

$$\kappa_{el} = \frac{1}{T}\left(\mathcal{L}^{(2)} - \frac{(\mathcal{L}^{(1)})^2}{\mathcal{L}^{(0)}}\right). \tag{12}$$

For bulk silicon, porous silicon and thin films, various temperature- and doping-dependent measurements are available [49–51, 12, 52]. It is well known that the lattice thermal conductivity of silicon is strongly dependent on temperature. While at room temperature a value of 87 W m^{-1} K^{-1} was reported, this value decreases to 36 W m^{-1} K^{-1} at 900 K and 23 W m^{-1} K^{-1} at 1200 K [12, 50], making silicon a high temperature thermoelectric. Even at high temperatures and applicable doping the electronic contribution to the thermal conductivity is only a few per cent of the total thermal conductivity. For bulk silicon it is reported that the heat conduction is impeded by higher dopant concentrations [51]. Here the lattice thermal conductivity reduction due to the scattering by dopant ions overbalances the increase of the electronic thermal conductivity. Due to this behavior the total thermal conductivity κ is weakly dependent on doping for temperatures clearly above 300 K [49, 52]. Nevertheless, for nanostructured silicon, e.g. in silicon-based superlattices [11, 53] or nanoparticle bulk silicon [12], with a low lattice thermal conductivity of $\kappa_{ph} < 3$ W m^{-1} K^{-1}, it may occur that the electronic thermal conductivity contributes remarkably to the total thermal conductivity. At high doping levels above 1×10^{20} cm^{-3} and temperature of 900 K the electronic contribution κ_{el} can be around 1–3 W m^{-1} K^{-1} and therefore approx. 25–50% of the total thermal conductivity. While it was recently shown [54, 11], that tensile strain could lead to a reduction of the thermal conductivity by up to 15% in bulk silicon as well as in silicon thin films, we did not

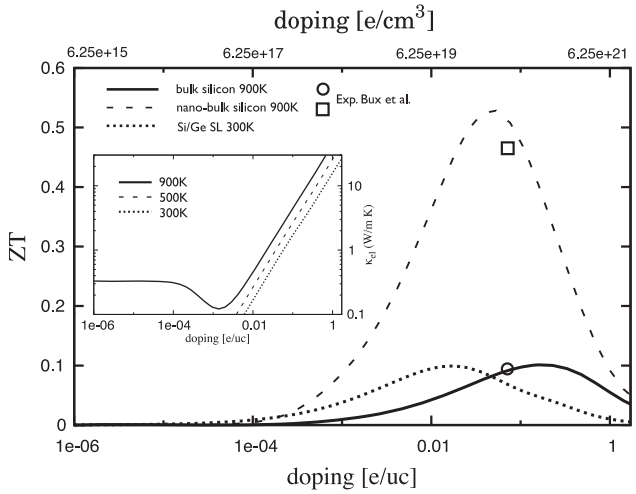

Figure 9. Calculated doping-dependent figure of merit for n-doped bulk silicon at 900 K (solid line), nanobulk silicon at 900 K (dashed line) and strained Si/Ge superlattice at 300 K (dotted line). The inset shows the doping-dependent electronic contribution to the total thermal conductivity for 300, 500 and 900 K. Experimental data (open square and circle) from [12] are given for comparison. Note the logarithmic axes.

include this in our estimation. In figure 9(a) the doping-dependent figure of merit for three silicon-based systems is shown. We assumed doping-independent experimental lattice thermal conductivities, stated for high doping rates, to include the reduction of κ_{ph} by ion scattering. Values of $\kappa_{ph} = 36$ W m^{-1} K^{-1} [12], $\kappa_{ph} = 3.8$ W m^{-1} K^{-1} [12] and $\kappa_{ph} = 1.9$ W m^{-1} K^{-1} [11] were used for single-crystalline bulk silicon, nanostructured bulk silicon and an Si/Ge superlattice, respectively. Here we consider only electron doping, which appeared to be most promising. The calculated doping-dependent electronic part κ_{el} is shown in the inset of figure 9 for three different temperatures. For bulk silicon (solid line in figure 9) we find a broad maximum for the figure of merit $ZT \approx 0.1$ at 900 K and high doping levels of $N \approx 6.5$–18×10^{20} cm^{-3}, which is in good agreement to experiments by Bux *et al* [12]. Compared to the related power factor (see figure 1) the maximum shifts to lower doping concentrations due to the linear increase of κ_{el} at higher doping rates, and therefore a stronger decrease of ZT at high doping rates. If a reduction of the lattice thermal conductivity can be achieved by nano-inclusions as reported in [12] a remarkable ZT of about 0.5 at $N = 3 \times 10^{20}$ cm^{-3} at 900 K could be obtained, making silicon an interesting high temperature thermoelectric (dashed line in figure 9). Nevertheless, at room temperature the lowest thermal conductivities have been stated for silicon- and germanium-based superlattices [11, 53]. Therefore the dotted line in figure 9 estimates the figure of merit for an Si/Ge superlattice with a period of 15 nm assuming no degradation of the electronic transport by the heterostructure. Here, at 300 K, the maximum figure of merit is found around doping levels of 7×10^{19} cm^{-3} with values of about 0.1, which are comparable to single-crystalline silicon at 900 K at ten times larger doping levels.

5. Conclusion

In conclusion, the thermoelectric transport properties of biaxially strained silicon were studied in detail with respect to a possible enhancement of the power factor. Two different doping and temperature regimes were analyzed in detail: a low doping ($N \approx 1 \times 10^{14}$ cm^{-3}) and low temperature regime ($T = 100$ K) suitable for metal-oxide–semiconductor device applications, and a heavy doping ($N \approx 1 \times 10^{20}$ cm^{-3}) and high temperature regime ($T = 900$ K) suitable for silicon-based thermoelectric modules.

It was shown that the electronic transport properties, namely the electrical conductivity σ and the thermopower S, are highly sensitive against strain. Nevertheless it was found that strain-induced effects in σ and S compensate each other, and no remarkable enhancement of the power factor by either compressive or tensile biaxial strain can be reached. On the other hand, a reduction of the power factor of up to 20% (30%) under electron (hole) doping due to the influence of strain was found. The latter was assigned to a large extent to band-structure-related redistribution of electrons. Estimations for the figure of merit under electron doping are given.

As a general result we showed that, when degenerate VBM or CBM exist, the thermopower decreases with deformation due to a redistribution of electrons in energetically lifted valleys. This could be the general explanation of the reduction of the electronic thermoelectric properties in strain-influenced heterostructures.

Acknowledgments

This work was supported by the Deutsche Forschungsgemeinschaft, SPP 1386 ‘Nanostrukturierte Thermoelektrika: Theorie, Modellsysteme und kontrollierte Synthese’. NFH is a member of the International Max Planck Research School for Science and Technology of Nanostructures. We want to thank Florian Rittweger for computational assistance.

References

[1] Snyder G J and Toberer E S 2008 Complex thermoelectric materials *Nature Mater.* **7** 105–14
[2] Sales B C 2002 Thermoelectric materials: smaller is cooler *Science* **295** 1248
[3] Majumdar A 2004 Thermoelectricity in semiconductor nanostructures *Science* **303** 777
[4] Böttner H, Chen G and Venkatasubramanian R 2006 Aspects of thin-film superlattice thermoelectric materials *MRS Bull.* **31** 211
[5] Venkatasubramanian R, Siivola E and Colpitts T 2001 Thin-film thermoelectric devices with high room-temperature figures of merit *Nature* **413** 597
[6] Harman T, Taylor P, Walsh M and LaForge B 2002 Quantum dot superlattice thermoelectric materials and devices *Science* **297** 2229
[7] Dresselhaus M, Chen G, Tang M and Yang R 2007 New directions for low-dimensional thermoelectric materials *Adv. Mater.* **19** 1
[8] Vining C B 2008 Materials science: desperately seeking silicon *Nature* **451** 132–3

[9] Hochbaum A, Chen R, Delgado R and Liang W 2008 Enhanced thermoelectric performance of rough silicon nanowires *Nature* **451** 163

[10] Boukai A I, Bunimovich Y, Tahir-Kheli J, Yu J K, Goddard W A III and Heath J R 2008 Silicon nanowires as efficient thermoelectric materials *Nature* **451** 168–71

[11] Lee S, Cahill D and Venkatasubramanian R 1997 Thermal conductivity of Si–Ge superlattices *Appl. Phys. Lett.* **70** 2957

[12] Bux S K, Blair R G, Gogna P K, Lee H, Chen G, Dresselhaus M S, Kaner R B and Fleurial J-P 2009 Nanostructured bulk silicon as an effective thermoelectric material *Adv. Funct. Mater.* **19** 2445–52

[13] Hao Q, Zhu G, Joshi G, Wang X, Minnich A, Ren Z and Chen G 2010 Theoretical studies on the thermoelectric figure of merit of nanograined bulk silicon *Appl. Phys. Lett.* **97** 063109

[14] Baykan M O, Thompson S E and Nishida T 2010 Strain effects on three-dimensional, two-dimensional, and one-dimensional silicon logic devices: predicting the future of strained silicon *J. Appl. Phys.* **108** 093716

[15] Prinz V and Golod S 2006 Elastic silicon-film-based nanoshells: formation, properties, and applications *J. Appl. Mech. Tech. Phys.* **47** 867

[16] Schmidt O and Eberl K 2001 Nanotechnology: thin solid films roll up into nanotubes *Nature* **410** 168

[17] Cho A 2006 Pretty as you please, curling films turn themselves into nanodevices *Science* **313** 164–5

[18] Ieong M, Doris B, Kedzierski J and Rim K 2004 Silicon device scaling to the sub-10 nm regime *Science* **306** 2057

[19] Fischetti M and Gamiz F 2002 On the enhanced electron mobility in strained-silicon inversion layers *J. Appl. Phys.* **92** 7320

[20] Giannozzi P *et al* 2009 QUANTUM ESPRESSO: a modular and open-source software project for quantum simulations of materials *J. Phys.: Condens. Matter* **21** 395502

[21] Mertig I 1999 Transport properties of dilute alloys *Rep. Prog. Phys.* **62** 237–76

[22] Perdew J P 1981 Self-interaction correction to density-functional approximations for many-electron systems *Phys. Rev.* B **23** 5048–79

[23] Corso A and Conte A 2005 Spin–orbit coupling with ultrasoft pseudopotentials: application to Au and Pt *Phys. Rev.* B **71** 115106

[24] Godby R W, Schlüter M and Sham L J 1988 Self-energy operators and exchange–correlation potentials in semiconductors *Phys. Rev.* B **37** 10159–75

[25] Varshni Y P 1967 Temperature dependence of the energy gap in semiconductors *Physica* **34** 149–54

[26] Vojta T, Mertig I and Zeller R 1992 Calculation of the residual resistivity and the thermoelectric power of sp impurities in silver *Phys. Rev.* B **46** 15761

[27] Thonhauser T, Scheidemantel T J and Sofo J O 2004 Improved thermoelectric devices using bismuth alloys *Appl. Phys. Lett.* **85** 588

[28] Yang J, Li H, Wu T and Zhang W 2008 Evaluation of half-heusler compounds as thermoelectric materials based on the calculated electrical transport properties *Adv. Funct. Mater.* **18** 2880

[29] Barth J, Fecher G H, Balke B, Ouardi S, Graf T, Felser C, Shkabko A, Weidenkaff A, Klaer P and Elmers H J 2010 *Phys. Rev.* B **81** 064404

[30] Singh D J 2010 Doping-dependent thermopower of PbTe from Boltzmann transport calculations *Phys. Rev.* B **81** 195217

[31] Parker D and Singh D 2010 High-temperature thermoelectric performance of heavily doped PbSe *Phys. Rev.* B **82** 035204

[32] May A F, Singh D J and Snyder G J 2009 Influence of band structure on the large thermoelectric performance of lanthanum telluride *Phys. Rev.* B **79** 153101

[33] Lee M-S, Poudeu F and Mahanti S 2011 Electronic structure and thermoelectric properties of Sb-based semiconducting half-Heusler compounds *Phys. Rev.* B **83** 085204

[34] Jacoboni C, Canali C, Ottaviani G and Quaranta A A 1977 A review of some charge transport properties of silicon *Solid-State Electron.* **20** 77–89

[35] Dziekan T, Zahn P, Meded V and Mirbt S 2007 Theoretical calculations of mobility enhancement in strained silicon *Phys. Rev.* B **75** 195213

[36] Roldán J B, Gámiz F, LópezVillanueva J A and Carceller J E 1996 A Monte Carlo study on the electron-transport properties of high-performance strained-Si on relaxed Si–Ge channel MOSFETs *J. Appl. Phys.* **80** 5121

[37] Mahan G and Sofo J 1996 The best thermoelectric *Proc. Natl Acad. Sci.* **93** 7436

[38] Lehmann G and Taut M 1972 On the numerical calculation of the density of states and related properties *Phys. Status Solidi* b **54** 469–77

[39] Zahn P, Mertig I, Richter M and Eschrig H 1995 *Ab initio* calculations of the giant magnetoresistance *Phys. Rev. Lett.* **75** 2996–9

[40] Mertig I, Mrosan E and Ziesche P 1987 *Multiple Scattering Theory of Point Defects in Metals: Electronic Properties* (Leipzig: B G Teubner)

[41] Ioffe A F 1960 *Physics of Semiconductors* (New York: Academic)

[42] Geballe T and Hull G 1955 Seebeck effect in silicon *Phys. Rev.* **98** 940

[43] Fulkerson W, Moore J, Williams R and Graves R 1968 Thermal conductivity, electrical resistivity, and seebeck coefficient of silicon from *Phys. Rev.* **167** 765

[44] Dugdale J S 1977 *The Electrical Properties of Metals and Alloys* (London: Edward Arnold)

[45] Cutler M and Mott N 1969 Observation of Anderson localization in an electron gas *Phys. Rev.* **181** 1336

[46] Yu D, Zhang Y and Liu F 2008 First-principles study of electronic properties of biaxially strained silicon: effects on charge carrier mobility *Phys. Rev.* B **78** 245204

[47] Nayak D K and Chun S K 1995 Low field hole mobility of strained Si on (100) $Si_{1-x}Ge_x$ substrate *Appl. Phys. Lett.* **64** 2514

[48] Sun G, Sun Y, Nishida T and Thompson S E 2007 Hole mobility in silicon inversion layers: stress and surface orientation *J. Appl. Phys.* **102** 084501

[49] Brinson M and Dunstant W 1970 Thermal conductivity and thermoelectric power of heavily doped n-type silicon *J. Phys. C: Solid State Phys.* **3** 483

[50] Shanks H, Maycock P, Sidles P and Danielson G 1963 Thermal conductivity of silicon from 300 to 1400 K *Phys. Rev.* **130** 1743–8

[51] Slack G A 2004 Thermal conductivity of pure and impure silicon, silicon carbide, and diamond *J. Appl. Phys.* **35** 3460

[52] Asheghi M, Kurabayashi K, Kasnavi R and Goodson K E 2002 Thermal conduction in doped single-crystal silicon films *J. Appl. Phys.* **91** 5079

[53] Borca-Tasciuc T 2000 Thermal conductivity of symmetrically strained Si/Ge superlattices *Superlatt. Microstruct.* **28** 199–206

[54] Li X, Maute K, Dunn M and Yang R 2010 Strain effects on the thermal conductivity of nanostructures *Phys. Rev.* B **81** 245318